Cell-type specific mechanical response and actomyosin dynamics in the developing *Drosophila* retina

Laura Blackie[1], Michael F. Staddon[2,3], Shiladitya Banerjee[2,3], & Franck Pichaud*[1,3]

[1] MRC Laboratory for Molecular Cell Biology, University College London, Gower Street, WC1E 6BT, London, United Kingdom.

[2] Department of Physics and Astronomy, University College London, Gower Street, WC1E 6BT, London, United Kingdom.

[3] Institute for the Physics of Living Systems, University College London, Gower Street, WC1E 6BT, London, United Kingdom.

*Corresponding author: f.pichaud@ucl.ac.uk

Phone: (+44) 0 207 679 7817

Fax: (+44) 0 207 679 7805

Keywords: Tissue patterning; heterogeneous cell shapes; *adherens junction* remodeling; actomyosin pulsation; computational modeling

Running title: Mechanical coupling during multicellular patterning

ABSTRACT

Organs consist of multiple cell types that assemble into multicellular structures, or physiological units, to support organ function. However, the mechanisms that regulate cell positioning and shape during physiological unit development remain elusive. To address this issue, we made use of the *Drosophila* ommatidium, which is the physiological unit of the retina. We show that during ommatidium assembly, the apical-medial cytosolic contractile actomyosin cytoskeleton plays a preeminent role in determining cell shape. In addition, we found that this contractile machinery underpins the capacity of cells to respond to mechanical perturbations. However, not all ommatidial cells are mechanically coupled. Our results argue that the ommatidial cells that present the highest velocity of Myosin-II particle displacement and the fastest area fluctuations during morphogenesis are also more prone than others to deformation in response to mechanical tension. Further, to understand the physical origin of the cell-type specific response to mechanical perturbation, we developed a tension-elasticity model for ommatidial shape. Using this model and by manipulating cell contractility, our work reveals that differences in cell mechanical properties can coordinate cell type specific shape dynamics.

INTRODUCTION

How genes encode cell and tissue geometry remains an outstanding question in cell and developmental biology. This question has mostly been studied in relatively simple epithelia such as the *Drosophila* wing (Classen et al., 2005)*,* or during instances of specific epithelial cell shape or tissue changes. These include cell apical constriction in the fly mesoderm (Martin et al., 2009a), vertebrate neural tube closure (Suzuki et al., 2012), cell intercalation in the *Drosophila* germband (Bertet et al., 2004; Blankenship et al., 2006) and epithelial spreading during zebrafish gastrulation (Lavoie et al., 2017). Patterning of simple epithelia, which often consist of one cell type, depends on the balance of contractile forces generated by the actomyosin cytoskeleton and intercellular adhesion (Heisenberg and Bellaiche, 2013; Lecuit and Yap, 2015; Munjal and Lecuit, 2014). As morphogenesis proceeds, individual cell heterogeneities tend to be ‘averaged out’ to produce a homogenous tissue, consisting of cells with very similar geometry (Farhadifar et al., 2007; Gibson et al., 2006). However most organs are complex tissues, which include different, complementary cell types. As a result, cell packing can be far from the typical hexagonal arrays described in simpler, more homogeneous tissues. How these different cell shapes and sizes are generated during multicellular patterning and what mechanisms mediate their persistence despite exposure to mechanical forces arising from concurrent cell morphogenetic programs is unclear. To address these questions we made use of the genetically tractable fly ommatidum, a stereotyped multicellular sensory unit that develops from multipotent retinal progenitors to adopt a crystal-like structure.

The *Drosophila* retina consists of approximately 750 identical physiological units called ommatidia. Each ommatidium comprises four glial-like cells, called the cone cells (CCs), surrounded by two epithelial primary pigment cells (PPCs) that are themselves surrounded by a ring of epithelial interommatidial cells (IOCs) (Ready, 1989). During ommatidium morphogenesis, all these cells acquire different geometries when considering their apical-junctional perimeter, and altogether assemble into a hexagonal lattice (Figure 1A). The developing ommatidium has long served as a model system for studying complex multicellular patterning during organogenesis due to its excellent genetic tractability and amenability to live imaging (Cagan, 2009; Carthew, 2005; Hayashi and Carthew, 2004; Larson et al., 2010). In particular, ommatidial patterning has served as a paradigm to study the role of developmentally controlled apoptosis (Freeman, 1996; Larson et al., 2010; Wolff and Ready, 1991) and preferential adhesion during multicellular patterning (Bao, 2014; Bao and Cagan, 2005; Bao et al., 2010; Beyer and Berthoud, 2018; Hayashi and Carthew, 2004; Hilgenfeldt et al., 2008; Kafer et al., 2007; Larson et al., 2010). Preferential heterophilic adhesion through the family of Immunoglobulin Neph (*Drosophila* Roughest, Kirre) - Nephrin-like (*Drosophila* Hibris, Sticks and Stones), between the PPCs and IOCs determines the positioning and shape of both PPCs and IOCs (Bao and Cagan, 2005; Bao et al., 2010). Additionally, Cadherin-based adhesion dictates the steady-state shape of the CCs (Hayashi and Carthew, 2004). While intercellular adhesion regulates the apical geometry of the CCs, PPCs and IOCs, it is not clear how adhesion relates to the contractile actomyosin cytoskeleton, which has not been extensively studied in these cells.

The epithelial actomyosin cytoskeleton includes two major pools - a cytosolic meshwork and filaments associated with the intercellular adhesion contacts *(Adherens Junction, AJ)*. The cytosolic meshwork can extend across the apical-medial plane, and is anchored to the *AJ* through discrete points of contact. It is pulsatile, with cycles of discrete node contraction and relaxation that can promote apical area fluctuations and *AJ* remodeling (Coravos et al., 2017). Pulses appear to be self-organizing and associated with cycles of phosphorylation and dephosphorylation of the Myosin-II regulatory light chain (Kasza et al., 2014; Mason et al., 2016; Munjal et al., 2015). The *AJ* pool of actomyosin is thought to function as part of a ratchet mechanism that can harness the contractile forces applied onto the *AJ* by the cytosolic meshwork to promote *AJ* remodeling during development (Coravos et al., 2017). In addition, it has been proposed that pulsed contraction of the actomyosin meshwork might be essential for preserving tissue integrity as cell constriction proceeds (Vasquez et al., 2016).

Here we combine molecular genetics, light-induced perturbation experiments as well as *in silico* modeling to investigate the role of the actomyosin cytoskeleton during ommatidium morphogenesis. We found that contractile actomyosin meshworks are present in the different ommatidial cell types. Our results show that these meshworks exhibit distinct cell-type specific properties and are essential for determining the apical-junctional geometry of the PPCs and IOCs, but not that of the CCs. Furthermore, our work reveals that these contractile meshworks respond to, and balance, forces across the developing ommatidium to promote multicellular patterning. Our computational model verifies that contractile meshworks determine the apical-junctional geometry of the PPCs and IOCs, which we find are mechanically coupled. This contrasts with the CCs, which our tension-elasticity model predicts are stiffer than the PPCs and IOCs. Consistent with this prediction, our results show that these cells are largely immune to mechanical forces generated by their neighbors.

RESULTS

Ommatidial cell types undergo distinct morphogenetic programs.

During ommatidium morphogenesis, the total apical area of the ommatidial core defined as the CCs and PPCs increases over time (Larson et al, 2010). To decipher the behavior of each individual retinal cell type over time, we quantified the apical area changes of the ommatidial cells using time-lapse imaging (Fichelson et al., 2012) (Figure 1B, Movie S1). These quantifications confirmed that the CCs, PPCs and IOCs all increase in apical area. However they do so at different rates (Figure 1C). Overall, apical area increase was gradual for all cell types, with an overall average rate of area change of 2.14+/-0.14 $\mu m^2/h$ for CCs, 8.92+/-0.47 $\mu m^2/h$ for PPCs and 2.52+/-1.43 $\mu m^2/h$ for IOCs (mean+/-standard deviation (S.D.)). Analysis of the relative contributions of the CCs, PPCs and IOCs to total ommatidial area demonstrated that while the percentage area contribution of the CCs and PPCs increases over time, that of the IOCs decreased as they narrowed and as cells are eliminated through developmentally regulated apoptosis (Figure 1D, Movie S1). Thus our results reveal that the CCs, PPCs and IOCs have different apical expansion rates, which indicates their differential mechanical properties.

Ommatidial cells undergo oscillations in apical area during morphogenesis.

Changes in junctional perimeter during epithelial cell morphogenesis have been shown to occur in a pulsatile manner in epithelia (Fernandez-Gonzalez and Zallen, 2011; Martin et al., 2009a; Sawyer et al., 2011). To test whether this is the case for ommatidial cells, we quantified cell apical area over short time scales during ommatidial morphogenesis. We found that while ommatidial cell types undergo cyclical fluctuations in apical area over a few minutes, differences exist in the median amplitude of these peaks of fluctuations that correlate with retinal cell-types (Figure 2A). PPCs exhibit the largest area fluctuations (Figure 2B), followed by IOCs then CCs (Figure 2C). In contrast, the median cycle length of pulses (defined as the time between subsequent peaks of area fluctuations) did not significantly differ between retinal cell-types (Figure 2D). The consistency of the median cycle length of fluctuations in area between CCs, PPCs and IOCs likely reflects the fact that the different cell types are mechanically coupled and indicates that mechanical coupling leads to a common basal frequency of apical area fluctuations over short time scales.

Actomyosin pulsation coordinates fluctuations in cell area.

During apical constriction and cell intercalation, cyclical area fluctuations that drive cell deformation have been linked to the pulsatile contractions in the cytosolic actomyosin meshworks (Fernandez-Gonzalez and Zallen, 2011; Martin et al., 2009b; Sawyer et al., 2011). In order to determine whether cytosolic contractile meshworks also regulate area fluctuation during ommatidium development, we examined the localization and dynamics of the actomyosin cytoskeleton in the maturing retinal cells using a GFP tagged version of the Myosin-II regulatory light chain, Sqh::GFP (Royou et al., 2002). These experiments revealed that Sqh::GFP localizes to the cell contacts and to a dynamic apical-medial meshwork in all ommatidial cells (Figure 3A, Movie S2). To characterize the dynamics of these meshworks, we generated kymographs along a line down the center of each cell (Figure 3B). The kymographs demonstrated that multiple peaks of MyoII intensity arise at different positions and at different time points in the cytosol of the CCs, PPCs and IOCs. We also found that the IOCs presented a higher density of MyoII peaks than PPCs or CCs (Figure 3B).

Next, we examined the specific pulsatile dynamics present in each ommatidial cell type using Particle Image Velocity (PIV) (Tseng et al, 2012). First, we calculated the average advection speed of MyoII and found that the velocity of Sqh::GFP motion varies between cell types and over time (Figure 3C). PPCs presented the highest median velocity followed by the IOCs and then the CCs. Examining the data over time showed that the median velocity of Sqh::GFP increases for all cell types as they are in the process of acquiring their apical-junctional geometry, and then decreases as they approach their mature shape (Figure 3C).

To approximate the contractility associated with the cytosolic actomyosin meshworks we calculated the divergence of the vector fields generated by PIV for Sqh::GFP. As ommatidial cells present large distributed meshworks (Figure 3A-B), we spatially averaged divergence dynamics over the whole apical area of each ommatidial cell type. With this approach, we found that contractility of cytosolic meshworks fluctuates in all ommatidial cells types with cyclical periods of contraction (pulse assembly, mean divergence < 0) and relaxation (pulse disassembly, mean divergence > 0) (Figure 3D). PPCs present lower median contraction/relaxation pulse amplitude than IOCs or CCs (Figure 3E). We also found that on average PPCs spent more time in a relaxed state over the observed developmental time period, whereas CCs spent more time in a contracted. IOCs spent a comparable amount of time either contracted or relaxed (Figure 3F). Furthermore, for all ommatidial cells, the median cycle length of fluctuations in MyoII contractility (Figure 3G) was comparable to that of the fluctuations in apical area (Figure 2D), suggesting that these parameters are correlated.

The similarity in cycle length of apical area fluctuations and in median cycle length of fluctuations in MyoII contractility are in good agreement with the notion that pulsatile contractions of the actomyosin meshwork can drive apical area fluctuations. To test this notion further, we analyzed ommatidia expressing Sqh::GFP and Ecad::Tomato to label the *AJ* perimeter. Visual inspection revealed that contraction of the actomyosin meshwork occurred in tandem with localized changes in cell apical area in PPCs (Figure 3H, Movie S3). Cross-correlating the fluctuations in ommatidial cell apical area over time with the fluctuations in MyoII contractility over time revealed a strong positive correlation between these two parameters for the PPCs and IOCs (Figure 3I-J). The strongest correlation occurred at an average time-lag of -31+/-9.7 s (mean+/-SEM) for the PPCs and -28.4+/-3.3 s for the IOCs. Thus, in these two cell types, the peak of actomyosin contractility precedes the maximum of apical area contraction (Figure 3I). Interestingly, the correlation between fluctuations in MyoII contractility and apical area fluctuations was not as strong for the CCs, suggesting that in these cells, pulsatile-contraction of the MyoII meshwork is less instructive for apical area change. Altogether our results are consistent with a role for the cytosolic contractile actomyosin meshwork in regulating cyclic deformation of the apical-junctional geometry of the PPCs and IOCs.

The contractile actomyosin meshwork regulates the shape of the PPCs.

To test the role of the actomyosin meshwork in cell deformation of the apical junctions more directly, we made use of a pulsed-IR laser to ablate individual actomyosin meshworks in ommatidial cells. We focused our work on the large and therefore more accessible PPCs (Figure 4A-C). Laser ablation within the medial-apical domain of a PPC triggered destabilization of the medial meshwork over the entire cell as monitored using Sqh::GFP (Figure 4B, Movie S4). To analyze the mechanical effect of these destabilizations on cell morphology, we quantified the change in cell apical area and shape over time. MyoII medial meshwork abrogation in a PPC was accompanied by an increase in the apical area of the targeted cell (Figure 4C-D, Movie S5). These experiments show that the pulsatile-contractile MyoII meshwork is necessary for maintaining the correct apical-junctional PPC geometry.

Ommatidial cells mount cell-type specific responses to mechanical perturbation.

When ablating one PPC, we noticed that the paired PPC constricted (Figure 4C-D), indicating that these two cells are mechanically coupled. To investigate this coupling more systematically, we sought to measure the deformation of the different ommatidial cell types when challenged by external mechanical perturbations. To this end, we quantified apical-junctional geometry by measuring the shape index $p = perimeter/\sqrt{area}$, which indicates the degree of shape anisotropy (Bi et al., 2014). For a regular hexagon, $p = 3.8$, and increases in magnitude as the shape becomes more elongated. This approach showed that the IOCs in direct contact with the targeted PPC cell deformed in shape but recovered their initial area (Figure 4D). Interestingly, the neighboring CCs did not show any change in apical area and apical-junctional geometry (Figure 4D-E), indicating that these cells are relatively immune to external mechanical perturbation. In contrast to the CCs, the non-targeted paired-PPC deformed significantly by shrinking in area and changing its apical-junctional geometry (Figure 4D-E). This deformation was accompanied by a sustained phase of cytosolic meshwork contraction (Movie S4 and Figure 4F), suggesting that these meshworks drive the changes in geometry. Altogether, these experiments indicate that the PPCs and IOCs are able to sense and respond to external forces through their contractile cytosolic actomyosin meshwork.

Mechanical model of the ommatidium predicts that differences in cell mechanical properties coordinate cell type specific shape dynamics.

To better understand the physical origin of the cell type specific mechanical response to actomyosin perturbations, we developed a two-dimensional *tension-elasticity* model of the ommatidium. This model is constructed based on vertex models for epithelial morphogenesis (Fletcher et al., 2014), where each cell is treated as a mechanical medium, carrying edge tensions at the cell-cell interfaces, a bulk tension arising from contractile medial actomyosin meshwork, and area elasticity penalizing changes in the cell apical area (Methods, Figure 5A). Competition between tension and elasticity gives rise to specific cell shapes, determined by parameters characterizing edge tension, bulk tension, and area elastic modulus (Figure 5A). Since we are interested in the overall morphology of the ommatidium and its relationship to cell-type specific properties, we treated the CC quartet as one mechanical object, PPCs as separate entities, and the left and right IOCs as individual mechanical objects. Starting with an initial circular configuration for the ommatidial cluster, we dynamically evolved the points on the cell contours based on their resultant forces, in order to obtain the steady-state morphology of the ommatidium (Figure 5B). The forces evolving ommatidium morphology result from minimizing the mechanical energy of the cluster (see Methods). We benchmarked the model parameters (tension parameters, elastic moduli) to recapitulate the shapes and sizes of the control CCs, IOCs and PPCs measured experimentally (Figure 1).

While our model accurately captured ommatidial cell morphologies, we sought to test if the model could capture the results of the laser ablation experiments (Figure 4). To simulate medial meshwork ablation in the PPC, we reduced the bulk tension in the left PPC, and allowed the cell cluster to dynamically evolve to a new morphology (Figure 5B). Our model quantitatively captured the experimentally measured morphological transformations provided that the elastic modulus of the CC cluster (k_c) is much higher than that of the IOC cluster (k_i) and the PPCs (k_{pp}), i.e. $k_c \gg k_i > k_{pp}$. Upon reduction in bulk contractility, the area of the targeted PPC expanded (Figure 5C) while decreasing its shape index (lower aspect ratio). In agreement with experimental data, the shape and size of the CC cluster remained unchanged, while the IOC cluster adjacent to the targeted PPC thinned in shape and recovered the initial drop in area over time (Figure 5C-D). The inclusion of a rigid CC cluster enabled mechanical communication between the PPCs, such that the untargeted PPC shrunk in area while increasing its shape index (higher aspect ratio). These results agree quantitatively with experiments and support the hypothesis for differential regulation of mechanical properties in the ommatidium.

To further test the predictive power of the model, we studied cell shape response to an increase in contractility (higher bulk tension) in the right PPC cell (Figure 5E). One prediction from the model is that increasing the tension of the medial meshwork in one PPC will cause the paired PPC to compensate by increasing its area (Figure 5F). Furthermore, our model predicted that the shape index should decrease for the paired PPC, and the IOCs, while increasing for the constricted PPC (Figure 5G). In order to test these predictions, we genetically increased medial meshwork tension by decreasing the expression of *sds22*, which encodes for the regulatory subunit of MyoII phosphatase PP1A (Grusche et al, 2009). We found that RNAi mediated knock down of *sds22* in one PPC displaced the equilibrium toward hyper-phosphorylation of MyoII, increasing contractility and resulting in a reduction in average apical area for the PPC (Figure 5H). Measurements of Sqh::GFP intensity within the *AJs* of *sds22*–deficient PPCs showed no significant difference to that measured in neighboring wild-type PPCs under these experimental conditions, suggesting this perturbation is relatively specific to the medial meshwork (Supplementary Figure 1). As predicted by the model, the decrease in PPC area was accompanied by a concomitant increase in average apical area of the paired PPC (Figure 5I-J). Altogether these results indicate that coupling between the two PPCs within the ommatidium can be achieved by differential stiffness between neighboring cell types. Specifically, our model predicts the central CC quartet should be stiffer than the surrounding PPCs and IOCs. Consistent with this prediction, staining retinas expressing Sqh::GFP shows that the CC quartet is delineated by a cable of A*J*-associated MyoII (Supplementary Figure 2). Taken together, our modeling and experimental manipulations suggest that the paired PPCs are mechanically balanced to absorb changes in forces thus allowing for robust patterning and to prevent damage propagation within the retinal lattice.

DISCUSSION

The actomyosin cytoskeleton plays a major role in regulating cell shape changes, such as cell apical constriction, which occur during epithelial tissue patterning. However, its broader role during organogenesis, which involves the concurrent morphogenesis of multiple cell types, is not well understood. Using the ommatidium as a model system, our work shows that apical-medial cytosolic actomyosin meshworks regulate the apical/*AJ* geometry of the PPCs and IOCs, through contractile forces. We find that during morphogenesis, these contractile machineries are at equilibrium. Interestingly, our work shows that a subset of cells, the CCs, do not deform when challenged by external mechanical coupling. Our theoretical model of the ommatidium predicts that this might be due to increased cortical stiffness in these cells. Altogether, our results indicate that the pulsatile-contractile meshwork is an essential driver of cell morphogenesis during heterogeneous tissue patterning. Our findings also suggest that cortical stiffness is an important parameter that can influence how mechanical forces are equilibrated across the multicellular structure.

The cytosolic actomyosin meshworks we have characterized in differentiating ommatidial cells differ from previously studied meshworks in that they do not seem to be polarized along any defined axis. In the fly mesoderm, cell apical constriction is powered by a radially polarized contractile meshworks (Martin et al., 2009a). In the germband, pulsatile flows of contractile actomyosin that are polarized along the anterior-posterior axis, drive *AJ* remodeling to promote cell intercalation (Rauzi et al., 2010). In ommatidial cells, the cytosolic contractile meshworks do not appear to be polarized and exhibit a continuous, distributed, fluctuating mesh through time and space. In contrast to the germband where intercalating cells maintain their area (Fernandez-Gonzalez and Zallen, 2011; Sawyer et al., 2011) or shrink as they constrict in the mesoderm (Martin et al., 2009a), we find that ommatidial cells gradually increase their area over time. Therefore, we propose that non-polarized cytosolic contractile meshworks can specifically regulate the geometry of apical-junctional cell profile without inducing a decrease in their area. As the IOCs differentiate, they acquire a narrow shape. Recent work in these cells has shown that during this process, morphogenesis of branched F-actin at the cell *AJ* counteract contractility in these cells (Del Signore et al., 2018). This counteracting effect prevents the total shrinkage of the corresponding *AJ*, so that instead it's length decreases. We therefore propose that the antagonistic action of the contractile cytosolic meshworks we report here, and *AJ* associated branched F-actin morphogenesis converge in regulating apical/*AJ* geometry of the PPCs and IOCs.

In addition, our laser induced mechanical perturbations and molecular genetic experiments show that amongst the ommatidial cells, the PPCs are the most responsive to local mechanical perturbations. These cells appear to be able to compensate for force imbalances by reducing their apical area. We propose that this property is linked to their low contraction/relaxation amplitude dynamics and high MyoII mean velocity. In particular, we envisage that a low contraction/relaxation amplitude dynamics might allow for these cells to mount a persistent response upon mechanical perturbation within the ommatidium. We speculate this property of the PPCs plays an important physiological role in that it might permit the insulation of defects that might arise during ommatidium morphogenesis, thus preventing them from propagating across the crystal-like retinal tissue.

Finally, both our perturbation experiments and mathematical model show that different cell types vary in their mechanical properties. In particular, the CCs do not deform easily when challenged with mechanical perturbation, even though these cells present a pulsatile actomyosin meshwork. One possibility is that these cells present a stiffer, less deformable cortex. This possibility is well supported by the fact that they are surrounded by an actomyosin cable. Interestingly, while we find that the CCs are relatively immune to mechanical perturbation, our work suggests that within their physiological unit they might limit the frequency of apical area fluctuations for the other ommatidial cell types. Cycle lengths have been reported before for other types of epithelial cells: germband cells have average apical areas of 40μm^2 and areas fluctuate with an average cycle length of 147.0+/-43.5s (Fernandez-Gonzalez and Zallen, 2011), mesoderm cells have an average apical area of 10-40µm^2 and an average cycle length of 82.8+/-48s (Martin et al., 2009) and amnioserosa cells have an average apical area of 100-200um^2 and an average cycle length of 230+/-76 secs (Solon et al., 2009). In the ommatidium, with its three distinct cell types, average apical areas vary from 43.4+/-14.2µm^2 for the PPCs, 9.4+/-1.8µm^2 for the IOCs and 5.9+/-3.0µm^2 for the CCs. Across the other tissues there appears to be a trend of larger cells having longer cycle lengths (Fernandez-Gonzalez and Zallen, 2011). The ommatidial cells fit this trend as they include cells of the smallest apical area and have the fastest median cycle length. However, the areas of the ommatidial cells fluctuate with the same median cycle length. This suggests that in the ommatidium, the smallest cells of the tissue set the cycle length for the larger cells. We hypothesize that such synchronization within a heterogeneous group of cells might be important for maintaining tissue integrity.

MATERIAL AND METHODS

Fly strains

Flies were raised on standard food at 25°C. Crosses were performed at 25°C. The following fly strains were used:

;Ecad::GFP; (Huang et al. (2009)

sqh^{AX3}*; sqh>sqhGFP;* (BL #57144, Royou et al. (2002))

;Ecad::Tomato; (Huang et al. (2009))

hsflp;;act>CD2>Gal4,UAS-RFP (BL #30558)

;UAS-sds22-RNAi (VDRC, 11788).

Time-lapse imaging

;Ecad::GFP; flies were staged to 15%APF at 25°C and the pupal case removed at the dorsal end to expose the retina. Pupae were mounted on blue-tac with the retina facing upwards and covered with a coverslip as described in (Fichelson et al., 2012). Time-lapse imaging was performed on a Zeiss inverted microscope with an Andor spinning disc using a Plan Neofluar 100x/1.3 Ph3 oil immersion objective. Images were acquired using ImageJ Micromanager software (Edelstein et al., 2014). Retinae were imaged for a minimum of 12h acquiring a Z-series in 1µm sections every 5m. Drift in XY and Z was corrected manually. Images were post processed in FIJI using the Stack-reg plugin (Thevenaz et al., 1998) to further correct for drift.

For imaging of medial meshwork dynamics, *sqh*^{AX3}*/Y;sqhGFP/EcadTomato;* flies were staged to 20%APF, 25%APF or 30%APF at 25°C and the pupal case pealed off to expose the retina. Pupae were mounted on blue-tac with the retinae facing upwards and covered with a coverslip. Retinae were imaged on a Zeiss LSM880 microscope with a Plan Apochromat 63x/NA1.4 oil objective using airyscan detectors. Images were acquired at a 40-45nm pixel size with a speed of 4.35s/frame. Airyscan processing was performed with the Zen software package to increase resolution.

Measurements of apical area over time

For measurements of the total apical area for each cell type, the outside perimeter of the CC cluster, PPCs and IOCs were traced manually using the Freehand selection tool in FIJI on every 20th frame (100mins) of the time-lapse of *;Ecad::GFP;* retinae. Areas were measured for each of the three rings over time and subtracted to generate values for each cell layer, then expressed as a percentage of the total ommatidium area. Measurements were averaged for each time point over 13 time-registered ommatidia from two independent retinae.

Particle Image Velocimetry (PIV)

Time lapse movies of *sqh*^{AX3}*/Y;sqhGFP/EcadTomato;* ommatidia were processed in Fiji with Bleach correction and Gaussian blur, and registered with the 'Stack-reg' plugin (Thevenaz et al., 1998) to correct for lateral drift. PIV analysis was performed using the FIJI PIV plugin (Tseng et al., 2012), by choosing an 8x8 pixel window with a time lag 4.34 seconds. Cell contours were tracked using the *Tissue Analyzer* plugin (Aigouy and Le Bivic, 2016) using FIJI, or manually in FIJI to segment the PPCs, IOCs and CCs. Further data analysis was performed in MATLAB with custom scripts. For calculation of the advection velocities of medial MyoII, the norms of the PIV vectors were averaged within each cell for each frame and divided by the frame rate. Advection speeds of each cell were then averaged in time for the Early (before CC intercalation), Mid (CC 4 way vertex) and Late stages (CC intercalation completed) of morphogenesis. Mean divergence of velocity vectors within each cell was calculated in MATLAB for each frame. Mean divergence, apical area and apical perimeter measurements over time, were processed by Gaussian smoothing with a window of 43s to improve the signal-to-noise ratio. Cycle lengths and peak amplitude were calculated in MATLAB using the 'findpeaks' command. Cross-correlation of the rate of area change and the rate of mean divergence change was performed in MATLAB for each cell and plotted as a heatmap.

Kymographs

Kymographs were generated using the Reslice plugin in FIJI along a 1 pixel wide segmented line that was drawn through the center of the cell and did not overlap with the *AJ*-associated MyoII in any frame. The movie presented in Figure 3 is of a *sqh*^{AX3}*; sqhGFP;* retina at the 'Late' stage of development imaged with a Zeiss LSM880 confocal with a Plan Apochromat 63x/NA1.4 oil objective using airyscan detectors drift corrected using the Stackreg plugin (Thévenaz et al., 1998) in FIJI.

Laser ablation

Ablations of MyoII cytosolic apical-medial meshworks were performed using a Zeiss LSM880 microscope with a Plan Apochromat 63x/NA1.4 oil objective, using 740nm multiphoton excitation from a Ti-sapphire laser. An ROI of 6x1 pixels for 30-40%APF retinae and 4x1 pixels for 20%APF retinae was drawn in the center of the apical region of the cell and targeted with a laser power of 10-20% at the slowest scan speed for 1 iteration. For monitoring the MyoII cytosolic apical-medial meshwork during ablation, *sqh*^{AX3}*/Y;sqhGFP/EcadTomato;* or *sqh*^{AX3}*/Y;sqhGFP;* flies were imaged using airyscan detectors. Images were acquired every 3.1-3.6s and processed with the Zen software. For quantification of area change after ablation, *;EcadGFP;* flies were used to visualize *AJs* and images were acquired every 1.27s before and after ablation.

Cell deformation after ablation

Cell deformations after ablation were analyzed on movies of *; EcadGFP ;* retinae where the PPC cytosolic apical-medial meshwork was targeted. Each cell type of interest was segmented manually using the Freehand Selection tool in FIJI on the initial frame before ablation and then every 10 frames (12.7s) until the maximum change in area was reached (normally about 200-250s). Area and perimeter/$\sqrt{\ }$area were measured and the ratio before and after ablation over time was calculated and averaged across 14 ommatidia.

Clonal analysis

To generate single cells deficient for *sds22*, *hs-flp;;actin>CD2>gal4,UAS-RFP* was crossed to *UAS-sds22-RNAi*. Flies were heat shocked at third instar larval stage at 37°C for 10-15min and dissected 4 days later.

Mechanical model for ommatidial morphology

The apical surface of the ommatidial cell cluster is modeled as a composite mechanical medium, consisting of an inner CC cluster of area A_c, a medial concentric layer of two adjacent PPC cells of areas A_{p1} and A_{p2}, and an outer layer of two IOC cell clusters of areas A_{i1} and A_{i2} (Figure 5A). In the spirit of vertex models (Farhadifar et al., 2007; Fletcher et al., 2014), each cellular unit (CCs, PPCs or IOCs) is characterized by a line tension, γ, at cell-cell interfaces; a surface tension, Γ, at their interiors; an elastic modulus, k, penalizing changes in cell apical area. The edge tension arises from a competition between intercellular adhesion and cortical actomyosin contractility, and the bulk tension arises from contractility in the medial actomyosin meshwork. The total mechanical energy of the cell colony is given by

$$E = \frac{k_c}{2}(A_c - A_{c0})^2 + \Gamma_c A_c + \frac{k_p}{2}(A_{p1} - A_{p0})^2 + \frac{k_p}{2}(A_{p2} - A_{p0})^2 + \Gamma_p\left(A_{p1} + A_{p2}\right)$$
$$+ \frac{k_i}{2}(A_{i1} - A_{i0})^2 + \frac{k_i}{2}(A_{i2} - A_{i0})^2 + \Gamma_i(A_{i1} + A_{i2}) + E_{int} \, ,$$

where k_c, k_p, and k_i define the areal elastic moduli of the CC, PPCs and IOC clusters, Γ_c, Γ_p, and Γ_i are the respective surface tensions, and A_{c0}, A_{p0}, and A_{i0} are the respective preferred areas of the three cell types. Intercellular interactions at cell-cell interfaces are given by the term E_{int}:

$$E_{int} = \sum_{\alpha,\beta} \gamma_{\alpha\beta} \, L_{\alpha\beta} \, ,$$

where $\gamma_{\alpha\beta}$ is the line tension at the interface between cell α and β $(\alpha, \beta \in \mathrm{CC}, \mathrm{PPC}, \mathrm{IOC})$ and $L_{\alpha\beta}$ is the length of the interface. Each point, $\vec{r}$, on the CC, IOC or PPC contour evolves in time according to the equation of motion

$$\mu \frac{\partial \vec{r}}{\partial t} = -\frac{\partial E}{\partial \vec{r}},$$

where μ is a friction coefficient. To account for pulsatile actomyosin oscillations we assume that cell surface tension fluctuates in time according to, $\Gamma_\alpha(t) = \Gamma_{\alpha 0}(1 + \theta \sin(\omega t + \varphi_\alpha))$, where α labels the cell type, $\Gamma_{\alpha 0}$ is the base tension, ω is the frequency of oscillations, and φ_α is a phase-shift calibrated from experimental data. The model is simulated using a custom code implemented using the Surface Evolver program (Brakke, 1992) starting with an initial circular morphology, consisting of an inner circular CC cluster, surrounded by concentric rings of PPC and IOC clusters. The model parameters are chosen to reproduce the experimentally measured geometry of the WT ommatidia (Table 1). To simulate medial meshwork ablation of cell α, we let $\Gamma_\alpha \to \Gamma_\alpha - \Delta\Gamma$, after relaxing the cell system to their mechanical equilibrium state. Similarly, to induce hyper-contractility we let $\Gamma_\alpha \to \Gamma_\alpha + \Delta\Gamma$ after mechanical relaxation.

Table 1. Model Parameters.

Cell type	**Preferred area**	**Surface tension Γ**	**Elastic modulus k**
PPC (left/right)	1.75	1.0	2.5
CC cluster	1.0	1.0	14.0
IOC cluster (left/right)	1.5	1.0	6.0

Interface type	**Edge tension γ**
CC-PPC	2.5
PPC-PPC	0.5
PPC-IOC	2.0
IOC-IOC	0.5
IOC-outside	2.0

Acknowledgments

We thank the Pichaud lab members, Rhian Walther for her help preparing the manuscript and Yanlan Mao and Melda Tozluoglu for their input during the course of this project. The N2 A71 anti-Armadillo antibody, was deposited to the DSHB by Wieschaus, E. (DSHB Hybridoma Product N2 7A1 Armadillo). Stocks obtained from the Bloomington *Drosophila* Stock Center (NIH P40OD018537) and the Vienna *Drosophila* Resource Center were used in this study. This work was funded by an MRC grant to FP (MC_UU_12018/3) and an MRC PhD studentship to LB. Work in SB lab is funded by Royal Society grant URF\R1\180187, and EPSRC funded PhD studentship to MFS.

Author contributions

FP conceived and supervised the work. LB designed, performed and analyzed the experiments. SB and LB developed analytical tools for experimental data analysis. SB and MFS designed and developed the computational model. FP and LB wrote the manuscript with the help of SB and RFW.

FIGURE LEGENDS

Figure 1: Ommatidial cell types concurrently undergo distinct morphogenetic programs.

(A) The arrangement of cells in the ommatidium. **(B-B'')** Snapshots taken from a time-lapse movie of ommatidium development with *AJs* labeled with endogenous Ecad::GFP. **(C)** Total apical area of each of the three cell layers over time (n=13 ommatidia). **(D)** Percentage apical area of each of the three cell layers relative to the apical area of the whole ommatidium over time (n=13 ommatidia). **(E)** Mean apical area of individual PPCs, CCs and IOCs at three different stages of morphogenesis. Error bars = standard deviation (S.D.)

Figure 2: Ommatidial cells undergo oscillations in area during morphogenesis.

(A) Apical area minus average apical area for each cell type over time for one PPC, CC and IOC. **(B)** Distribution of apical area minus average apical area for PPCs, CCs and IOCs (n=9 ommatidia). **(C)** Amplitude of peaks in area fluctuations for PPCs, CCs and IOCs (n=9 ommatidia, Kruskal-Wallis test, p<0.0001, post-hoc Dunn’s multiple comparisons tests: PPC-CC p<0.0001, PPC-IOC p<0.0001, CC-IOC p=0.0004). **(D)** Cycle length of peaks in area fluctuations for PPCs, CCs and IOCs (n=9 ommatidia, Kruskal-Wallis test, p=0.1708). Error bars = median and interquartile range

Figure 3: Actomyosin pulsation coordinates changes in cell area.

(A) *sqh*^{AX3}*;sqhGFP;* ommatidium showing that MyoII localizes to an extensive medial meshwork across all cell types. IOCs are outlined in black, the PPCs in green and CCs in turquoise. High-intensity MyoII meshworks are outlined by a dashed line in the PPCs. **(B)** Kymographs showing MyoII intensity along a line through the center of each cell, indicated by red line in diagram, for each cell type over time along the X-axis. **(C)** Median velocity of MyoII medial meshwork at each stage of morphogenesis for PPCs, CCs and IOCs (n=9 ommatidia, Kruskal-Wallis and Dunn’s post-hoc tests, p<0.0001 for all tests except Early PPC-IOC where p=0.5545). **(D)** Contractility (mean divergence) over time for one PPC, CC and IOC. **(E)** Amplitudes of peaks in contractility fluctuations for PPCs, CCs and IOCs (n=9 ommatidia, Kruskal-Wallis test, p<0.0001, Dunn’s post-hoc tests: PPC-CC p=0.0145, PPC-IOC p<0.0001, CC-IOC p=0.0727). **(F)** Continuous time spent relaxed or contracted for PPCs, CCs and IOCs (n=9 ommatidia, Kruskal-Wallis test, p<0.0001, post-hoc Dunn’s multiple comparisons tests: PPC relaxed-PPC contracted p=0.0007, CC relaxed-CC contracted p<0.0001, IOC relaxed-IOC contracted p=0.4585). **(G)** Cycle length of peaks in contractility fluctuations for PPCs, CCs and IOCs (n=9 ommatidia, Kruskal-

Wallis test, p=0.053). **(H)** High magnification images of a pulse of MyoII assembling and disassembling in a PPC. MyoII is labelled with SqhGFP (green) and *AJs* are labeled with Ecad::Tomato (red). The *AJ* of the PPC is outlined with a dashed line. A turquoise line outlines the *AJ* at the onset of contraction and is used for reference in the subsequent panels. A white dashed line is then used to outline the *AJ* as the cell undergo local pulsed-contraction. Note how PPC contracts as a MyoII pulse assembles and then relaxes as the pulse disassembles. **(I)** Heatmap showing temporal cross-correlation for multiple PPCs, CCs and IOCs. Each row represents an individual cell (n=9 ommatidia). Error bars = Median and interquartile range. (**J**) Temporal cross-correlations of MyoII contractility fluctuations with area fluctuations for cell shown in (H).

Figure 4: Ommatidial cells mount cell-type specific responses to mechanical perturbation.

(A) Diagram of position of quantified cells relative to medial meshwork ablation (red asterisk). **(B)** Time-course showing response of cells after medial meshwork ablation in left PPC. MyoII is labelled by SqhGFP (green). Red star indicates point of laser ablation. Cell shapes are outlined in white on first frame and overlaid on subsequent frames to indicate cell shape changes. **(C)** Time-course showing *AJs* labeled with Ecad::GFP after ablation of the medial meshwork in left PPC. Region of ablation marked with red star. Cell outlines before ablation superimposed on each image with green dotted line. IOC outlined in magenta. **(D)** Apical area change over time after ablation, $A_{(T)}/A_{(0)}$, A=apical area (n=14 ommatidia). **(E)** Cell shape index (perimeter/ $\sqrt{\ }$area) relative to initial shape parameter over time after ablation (n=14 ommatidia). **(F)** Average length of the first MyoII contraction pulse after ablation (n=5 ommatidia, one-way ANOVA p=0.0005, PPC compared to CC, IOC, control IOC: $p<0.05$; other comparisons: n.s.) Error bars: D,E) = S.E.M., I) = S.D.

Figure 5: Mechanical model of the ommatidial cluster predicts cell type specific mechanical response.

(A) Schematic of the tension-elasticity model of the ommatidial cluster, showing the edge tensions, bulk elasticity parameters in the CC cluster (blue), PPCs (green) and the IOC cell clusters (red). **(B)** Simulations of ablation experiments by reducing bulk tension in one of the PPC cells (marked by an asterix). Left to right: evolution of colony morphology upon ablation. **(C)** Model prediction for the dynamics of the apical area (normalized) for the different cell clusters in the ommatidia, upon ablation at $t = 0$. **(D)** Model prediction for the dynamics of the cell shape index (perimeter/$\sqrt{}$ area, normalized) for the different cell clusters in the ommatidia, upon ablation at $t = 0$. **(E)** Simulation of the hypercontraction in the right PPC (marked by asterix). **(F)** Model prediction for the dynamics of the apical area (normalized) for the different cell clusters in the ommatidia, upon the induction of hyper-contraction in the right PPC at $t = 0$. **(G)** Model prediction for the dynamics of the cell shape index (perimeter/$\sqrt{}$ area, normalized) for the different cell clusters in the ommatidia, upon the induction of hyper-contraction in the right PPC at $t = 0$. **(H)** Single PPC HS clone expressing *sds22-RNAi*. Clone marked by the presence of mCherry. **(I)** Area of PPCs expressing *sds22-RNAi*, wild-type PPCs in the same ommatidia and wild-type PPCs in unaffected ommatidia (n= 176, 176, 254 ommatidia respectively, one-way ANOVA, p<0.0001). **(J)** Cell shape index (perimeter/$\sqrt{}$ area) of PPCs expressing *sds22-RNAi*, wild-type PPCs in the same ommatidia and wild-type PPCs in unaffected ommatidia (n= 176, 176, 254 ommatidia respectively, one-way ANOVA, p=0.0071, sds22-RNAi-paired p=0.0048, *sds22RNAi*-wild-type p=0.2880, paired-wild-type p=0.1346). Error bars = S.D.

Figure S1: *sds22-RNAi* does not affect the *AJ* pool of MyoII

(A) MyoII intensity on the PPC-IOC *AJ* for WT and *sds22RNAi* expressing cells paired by ommatidia.

Figure S2: The CC quartet is delineated by a cable of actomyosin

(A) Ommatidium from a *sqh*^{AX}*;sqhGFP;* retina stained for Arm (Red).

REFERENCES

Aigouy, B. and Le Bivic, A. (2016). The PCP pathway regulates Baz planar distribution in epithelial cells. *Sci Rep* **6**, 33420.
Bao, S. (2014). Notch controls cell adhesion in the Drosophila eye. *PLoS Genet* **10**, e1004087.
Bao, S. and Cagan, R. (2005). Preferential adhesion mediated by Hibris and Roughest regulates morphogenesis and patterning in the Drosophila eye. *Dev Cell* **8**, 925-935.
Bao, S., Fischbach, K. F., Corbin, V. and Cagan, R. L. (2010). Preferential adhesion maintains separation of ommatidia in the Drosophila eye. *Dev Biol* **344**, 948-956.
Bertet, C., Sulak, L. and Lecuit, T. (2004). Myosin-dependent junction remodelling controls planar cell intercalation and axis elongation. *Nature* **429**, 667-671.
Beyer, E. C. and Berthoud, V. M. (2018). Gap junction gene and protein families: Connexins, innexins, and pannexins. *Biochim Biophys Acta* **1860**, 5-8.
Bi, D., Lopez, J. H., Schwarz, J. M. and Manning, M. L. (2014). Energy barriers and cell migration in densely packed tissues. *Soft matter* **10**, 1885-1890.
Blankenship, J. T., Backovic, S. T., Sanny, J. S., Weitz, O. and Zallen, J. A. (2006). Multicellular rosette formation links planar cell polarity to tissue morphogenesis. *Dev Cell* **11**, 459-470.
Brakke, K. A. (1992). The Surface Evolver. *Experimental Mathematics* **1**, 14.
Cagan, R. (2009). Principles of Drosophila eye differentiation. *Curr Top Dev Biol* **89**, 115-135.
Carthew, R. W. (2005). Adhesion proteins and the control of cell shape. *Curr Opin Genet Dev* **15**, 358-363.
Classen, A. K., Anderson, K. I., Marois, E. and Eaton, S. (2005). Hexagonal packing of Drosophila wing epithelial cells by the planar cell polarity pathway. *Dev Cell* **9**, 805-817.
Coravos, J. S., Mason, F. M. and Martin, A. C. (2017). Actomyosin Pulsing in Tissue Integrity Maintenance during Morphogenesis. *Trends Cell Biol* **27**, 276-283.
Del Signore, S. J., Cilla, R. and Hatini, V. (2018). The WAVE Regulatory Complex and Branched F-Actin Counterbalance Contractile Force to Control Cell Shape and Packing in the Drosophila Eye. *Dev Cell* **44**, 471-483 e474.
Farhadifar, R., Roper, J. C., Aigouy, B., Eaton, S. and Julicher, F. (2007). The influence of cell mechanics, cell-cell interactions, and proliferation on epithelial packing. *Curr Biol* **17**, 2095-2104.
Fernandez-Gonzalez, R. and Zallen, J. A. (2011). Oscillatory behaviors and hierarchical assembly of contractile structures in intercalating cells. *Phys Biol* **8**, 045005.

Fichelson, P., Brigui, A. and Pichaud, F. (2012). Orthodenticle and Kruppel homolog 1 regulate Drosophila photoreceptor maturation. *Proc Natl Acad Sci U S A* **109**, 7893-7898.

Fletcher, A. G., Osterfield, M., Baker, R. E. and Shvartsman, S. Y. (2014). Vertex models of epithelial morphogenesis. *Biophys J* **106**, 2291-2304.

Freeman, M. (1996). Reiterative use of the EGF receptor triggers differentiation of all cell types in the Drosophila eye. *Cell* **87**, 651-660.

Gibson, M. C., Patel, A. B., Nagpal, R. and Perrimon, N. (2006). The emergence of geometric order in proliferating metazoan epithelia. *Nature* **442**, 1038-1041.

Hayashi, T. and Carthew, R. W. (2004). Surface mechanics mediate pattern formation in the developing retina. *Nature* **431**, 647-652.

Heisenberg, C. P. and Bellaiche, Y. (2013). Forces in tissue morphogenesis and patterning. *Cell* **153**, 948-962.

Hilgenfeldt, S., Erisken, S. and Carthew, R. W. (2008). Physical modeling of cell geometric order in an epithelial tissue. *Proc Natl Acad Sci U S A* **105**, 907-911.

Kafer, J., Hayashi, T., Maree, A. F., Carthew, R. W. and Graner, F. (2007). Cell adhesion and cortex contractility determine cell patterning in the Drosophila retina. *Proc Natl Acad Sci U S A* **104**, 18549-18554.

Kasza, K. E., Farrell, D. L. and Zallen, J. A. (2014). Spatiotemporal control of epithelial remodeling by regulated myosin phosphorylation. *Proc Natl Acad Sci U S A* **111**, 11732-11737.

Larson, D. E., Johnson, R. I., Swat, M., Cordero, J. B., Glazier, J. A. and Cagan, R. L. (2010). Computer simulation of cellular patterning within the Drosophila pupal eye. *PLoS computational biology* **6**, e1000841.

Lavoie, J., Gasso Astorga, P., Segal-Gavish, H., Wu, Y. C., Chung, Y., Cascella, N. G., Sawa, A. and Ishizuka, K. (2017). The Olfactory Neural Epithelium As a Tool in Neuroscience. *Trends in molecular medicine* **23**, 100-103.

Lecuit, T. and Yap, A. S. (2015). E-cadherin junctions as active mechanical integrators in tissue dynamics. *Nat Cell Biol* **17**, 533-539.

Martin, A. C., Kaschube, M. and Wieschaus, E. F. (2009a). Pulsed contractions of an actin-myosin network drive apical constriction. *Nature* **457**, 495-499.

Martin, R., Smibert, P., Yalcin, A., Tyler, D. M., Schafer, U., Tuschl, T. and Lai, E. C. (2009b). A Drosophila pasha mutant distinguishes the canonical microRNA and mirtron pathways. *Mol Cell Biol* **29**, 861-870.

Mason, F. M., Xie, S., Vasquez, C. G., Tworoger, M. and Martin, A. C. (2016). RhoA GTPase inhibition organizes contraction during epithelial morphogenesis. *J Cell Biol* **214**, 603-617.

Munjal, A. and Lecuit, T. (2014). Actomyosin networks and tissue morphogenesis. *Development* **141**, 1789-1793.

Munjal, A., Philippe, J. M., Munro, E. and Lecuit, T. (2015). A self-organized biomechanical network drives shape changes during tissue morphogenesis. *Nature* **524**, 351-355.

Rauzi, M., Lenne, P. F. and Lecuit, T. (2010). Planar polarized actomyosin contractile flows control epithelial junction remodelling. *Nature* **468**, 1110-1114.

Ready, D. F. (1989). A multifaceted approach to neural development. *Trends Neurosci* **12**, 102-110.

Royou, A., Sullivan, W. and Karess, R. (2002). Cortical recruitment of nonmuscle myosin II in early syncytial Drosophila embryos: its role in nuclear axial expansion and its regulation by Cdc2 activity. *J Cell Biol* **158**, 127-137.

Sawyer, J. K., Choi, W., Jung, K. C., He, L., Harris, N. J. and Peifer, M. (2011). A contractile actomyosin network linked to adherens junctions by Canoe/afadin helps drive convergent extension. *Mol Biol Cell* **22**, 2491-2508.

Suzuki, M., Morita, H. and Ueno, N. (2012). Molecular mechanisms of cell shape changes that contribute to vertebrate neural tube closure. *Development, growth & differentiation* **54**, 266-276.

Thevenaz, P., Ruttimann, U. E. and Unser, M. (1998). A pyramid approach to subpixel registration based on intensity. *IEEE Trans Image Process* **7**, 27-41.

Tseng, Q., Duchemin-Pelletier, E., Deshiere, A., Balland, M., Guillou, H., Filhol, O. and Thery, M. (2012). Spatial organization of the extracellular matrix regulates cell-cell junction positioning. *Proc Natl Acad Sci U S A* **109**, 1506-1511.

Vasquez, C. G., Heissler, S. M., Billington, N., Sellers, J. R. and Martin, A. C. (2016). Drosophila non-muscle myosin II motor activity determines the rate of tissue folding. *Elife* **5**.

Wolff, T. and Ready, D. F. (1991). Cell death in normal and rough eye mutants of Drosophila. *Development* **113**, 825-839.

Figure 1: Ommatidial cell types undergo distinct morphogenetic programs

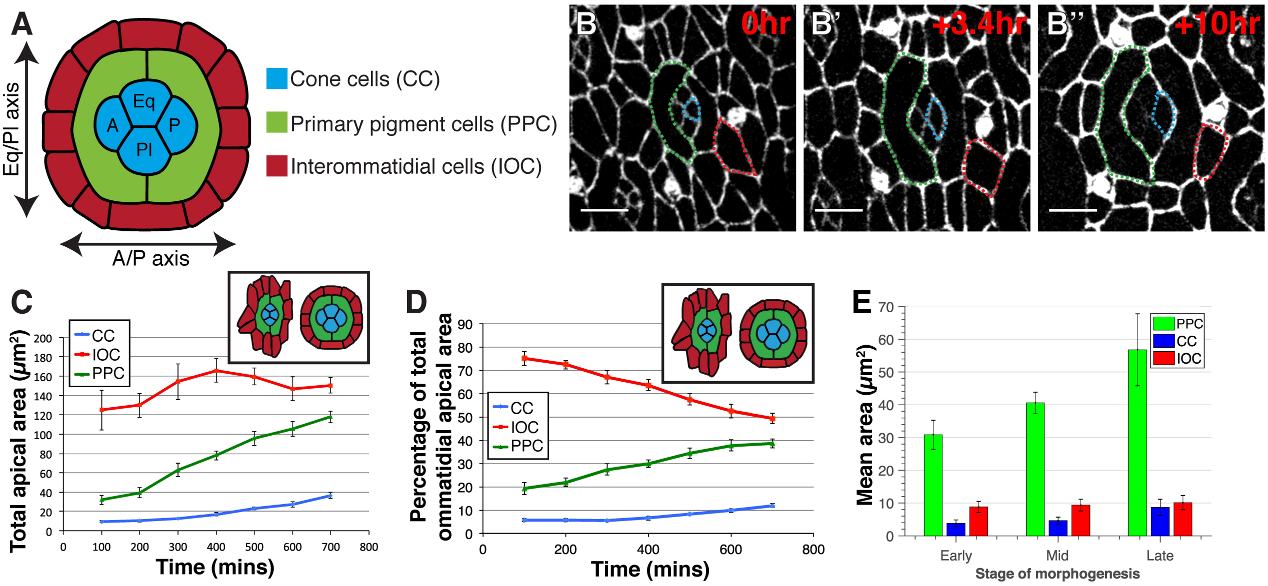

Figure 2: Ommatidial cells undergo oscillations in apical area during morphogenesis

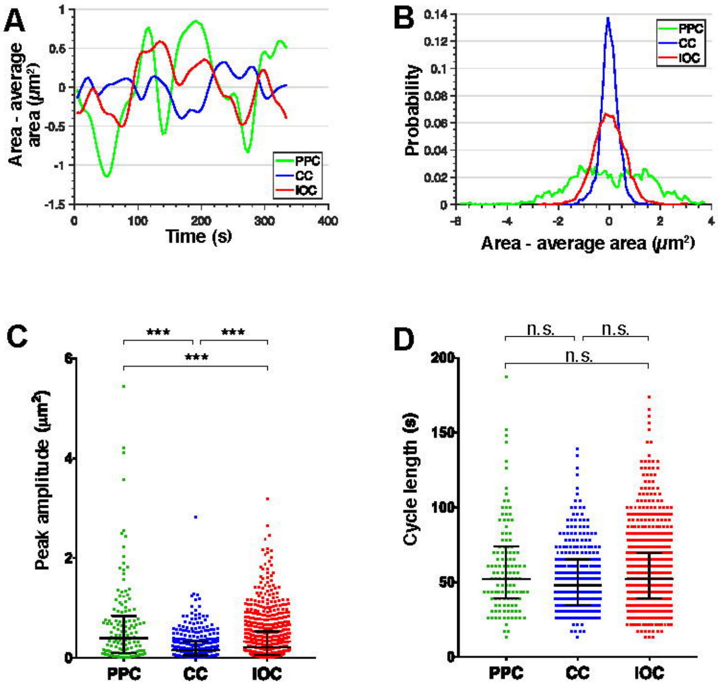

Figure 3: Actomyosin pulsation coordinates fluctuation in cell area in the ommatidium

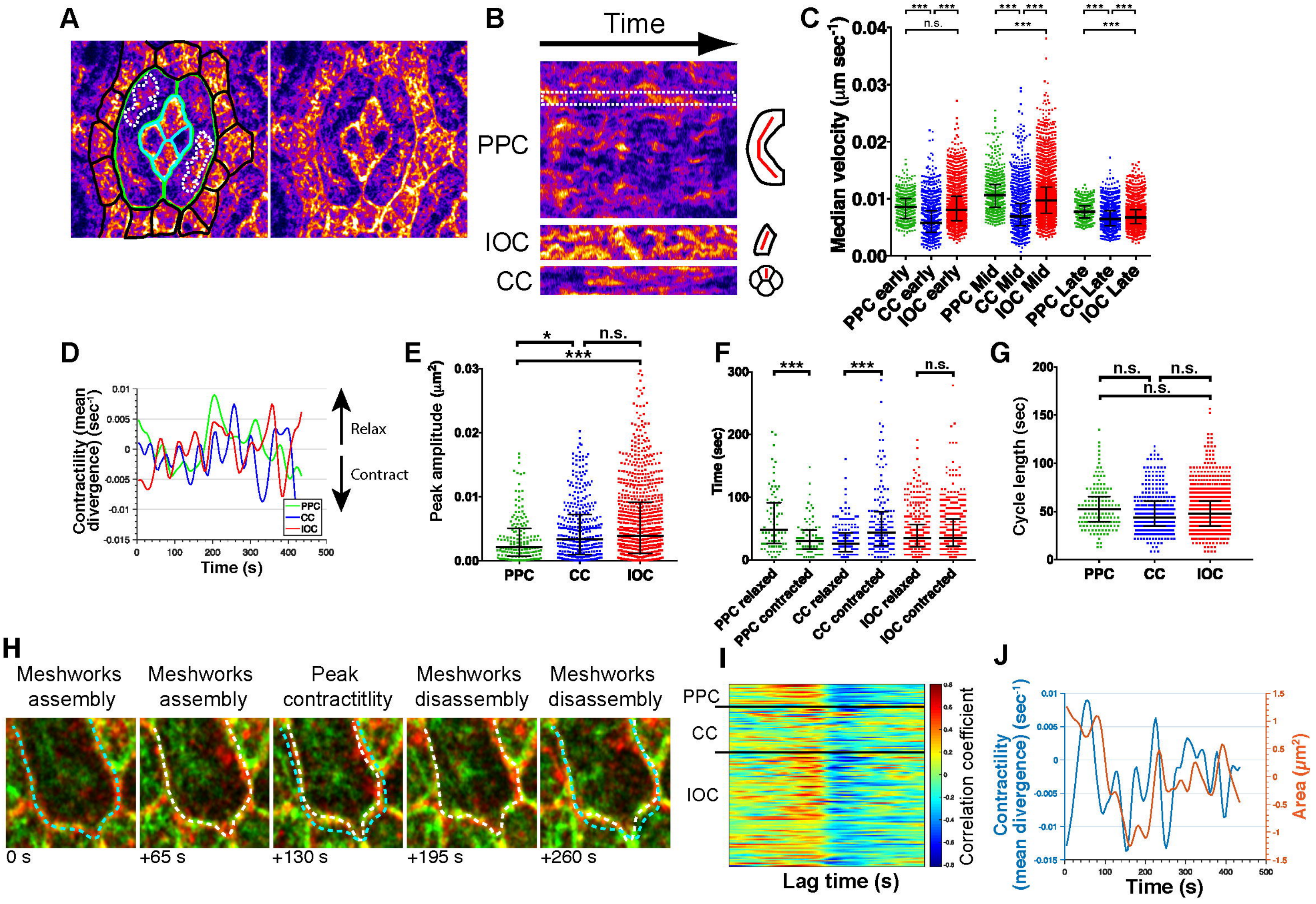

Figure 4: Ommatidial cells mount cell-type specific responses to mechanical perturbation

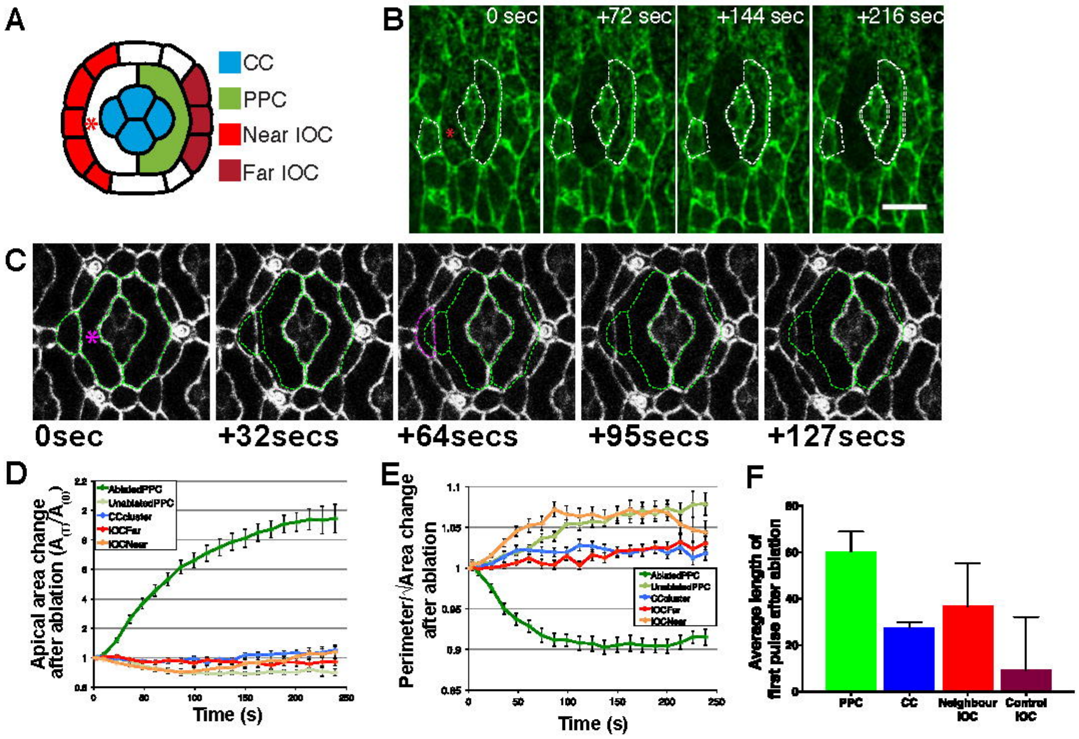

Figure 5: Tension-elasticity model of the developing ommatidium